



## Microstructure, mechanical properties and incipient plasticity of $(\text{Ti}_{42.5}\text{Zr}_{42.5}\text{Nb}_{10}\text{Ta}_5)_{100-x}\text{Mo}_x$ refractory high-entropy alloys

Jiaqing Qin<sup>a,b</sup>, Yanliang Yi<sup>b,c, \*\*</sup>, Shaolei Long<sup>d, \*\*\*</sup>, Min Ling<sup>d</sup>, Liqiong Zhong<sup>e</sup>, Fengshuo Jin<sup>b</sup>, Juan Han<sup>b</sup>, Weiji Lai<sup>a,\*</sup>

<sup>a</sup> Guangdong Provincial Key Laboratory of Spine and Spinal Cord Reconstruction, The Fifth Affiliated Hospital (Heyuan Shenhe People's Hospital), Jinan University, Heyuan, 517000, China

<sup>b</sup> Institute of Advance Wear & Corrosion Resistant and Functional Materials, Jinan University, Guangzhou, Guangdong, 510632, China

<sup>c</sup> Shaoguan Research Institute of Jinan University, Shaoguan, 512027, Guangdong, China

<sup>d</sup> School of Mechanical Engineering, Guizhou Institute of Technology, Guiyang, Guiyang, 550003, China

<sup>e</sup> College of Mechanical Engineering, Guiyang University, Guiyang, Guiyang, 550005, China



### ARTICLE INFO

#### Keywords:

Refractory high-entropy alloy  
Microstructure  
Mechanical properties  
Nanoindentation

### ABSTRACT

A series of  $(\text{Ti}_{42.5}\text{Zr}_{42.5}\text{Nb}_{10}\text{Ta}_5)_{100-x}\text{Mo}_x$  ( $x = 0, 3, 5$  and  $7$  at.%) refractory high-entropy alloys (RHEAs) were prepared, and the influence of Mo content on microstructure and mechanical properties of the RHEAs were systematically studied. All the RHEAs consist of a single body-centered cubic (BCC) phase. As the Mo content increases from 0 at.% to 7 at.%, the yield strength of RHEAs increases from 670 MPa to 975 MPa at room temperature. The high strength of the BCC RHEAs mainly depends on solid-solution strengthening caused by the Mo addition. The RHEAs with low Mo content (0–5 at.%) can possess high tensile plasticity of ~20 %, while it reflects brittle after the 7 at.% Mo addition. The high tensile plasticity of the RHEAs was attributed to the combined effects of lattice rotation to promote and refine crystalline strengthening. The RHEAs with 5 at.% Mo addition have high specific yield strength (~32 MPa g<sup>-1</sup> cm<sup>3</sup>) and excellent fracture strains (> 60 %) at 1173 K. Moreover, the incipient plasticity of the RHEAs was analyzed by nanoindentation. It is shown that the maximum shear stress ( $\tau_{\max}$ ) of the RHEAs from 1.80–2.34 GPa to 2.67–4.83 GPa. The activation volumes ( $v^*$ ) of the RHEAs from 0.7  $\Omega$  to 1.1  $\Omega$ . The nanomechanical properties of the RHEAs are related to the Mo content. The purpose of this work is to design RHEAs with excellent mechanical properties and to offer a theoretical foundation to assist new RHEA design.

### 1. Introduction

As contemporary machinery updates, the high-temperature materials serviced in aerospace and nuclear reactors urgent need higher and higher service temperature and efficiency. However, traditional superalloys cannot meet these needs due to insufficient mechanical properties at high temperatures. For example, the strengths of Ni-based superalloys are about 1000 MPa at room temperature, while they are about 200 MPa at 1000 °C [1,2]. Generally, increasing the melting point of an alloy can improve its maximum working temperature [3,4]. Consequently, it is of great significance to explore the superalloy composed of elements with

high melting points.

For the past few years, researchers proposed refractory high-entropy alloys (RHEAs) from the perspective of “entropy parameters”, which are mainly composed of Mo, Nb, Hf, Zr, and Ti elements, etc [5,6]. The RHEAs with excellent high-temperature mechanical properties mostly depend on the characteristics of high-entropy, lattice distortion, hysteresis diffusion and cocktail effects [7]. For example, the yield strengths of NbMoTaW and VNbMoTaW RHEAs can reach 410 and 630 MPa at 1400 °C, respectively [8]. To ensure successful industrialization, improving strength and plasticity of RHEAs at room temperature remains a top priority.

\* Corresponding author. Guangdong Provincial Key Laboratory of Spine and Spinal Cord Reconstruction, The Fifth Affiliated Hospital (Heyuan Shenhe People's Hospital), Jinan University, Heyuan, 517000, China.

\*\* Corresponding author. Institute of Advance Wear & Corrosion Resistant and Functional Materials, Jinan University, Guangzhou, Guangdong, 510632, China

\*\*\* Corresponding author. School of Mechanical Engineering, Guizhou Institute of Technology, Guiyang, Guiyang, 550003, China.

E-mail addresses: [y Yanliang@163.com](mailto:y Yanliang@163.com) (Y. Yi), [20180875@git.edu.cn](mailto:20180875@git.edu.cn) (S. Long), [lwj9279@163.com](mailto:lwj9279@163.com) (W. Lai).

Recently, numerous researches had demonstrated that altering chemical composition could effectively promote the mechanical properties of RHEAs [9]. Han et al. [10] found that 20 at.% Ti addition could significantly improve the plasticity of NbMoTaW RHEA, and the compressive plastic strain of RHEA increased from 2.6% to 10.6%. Khan et al. [11] combined refractory elements Nb and Ta with Ti, Zr and Al, resulting in  $(\text{TiNbBr})_{89}(\text{AlTa})_{11}$  RHEA with excellent mechanical properties, including a compressive yield strength of  $\sim 890$  MPa and excellent plasticity of  $\sim 70\%$  at 298 K. Lee et al. [12] reported the NbTaTiV RHEA doped by the 20 at.% Zr, of which the yield strength increased from 1239 MPa to 1518 MPa. Wang et al. [13] revealed that the lattice distortion caused by Mo addition significantly facilitated the strength of  $(\text{TiZrNbTa})_{100-x}\text{Mo}_x$  ( $0 \leq x \leq 20$ ) RHEAs, of which the yield strength increased from  $\sim 1020$  MPa to  $\sim 1450$  MPa. Among the constituent elements (Ti, Zr, Nb, V, Mo and Ta, etc), Mo element has a larger atomic radius and electronegativity [14], higher melting point and Young's modulus [15], which can better improve the solid-solution strengthening [16], interatomic bonding [17] and high-temperature mechanical properties [18] of RHEAs. However, excessive Mo addition might lead to the formation of new phases, while insufficient Mo content cannot optimize the mechanical properties to the maximum extent [19].

In this work, a series of  $(\text{Ti}_{42.5}\text{Zr}_{42.5}\text{Nb}_{10}\text{Ta}_5)_{100-x}\text{Mo}_x$  ( $x = 0, 3, 5$  and  $7$  at.%) RHEAs were prepared, and the effect of Mo content on microstructure, mechanical properties and nanomechanical properties of the RHEAs was systematically analyzed. The purpose of this work is to design RHEAs with excellent mechanical properties and to determine optimal solution of Mo additive content in RHEAs. This study not only provides insights into understanding mechanical properties of RHEAs but also offers a theoretical foundation to assist new RHEAs design.

## 2. Materials preparation and characterization

### 2.1. Materials preparation

The  $(\text{Ti}_{42.5}\text{Zr}_{42.5}\text{Nb}_{10}\text{Ta}_5)_{100-x}\text{Mo}_x$  ( $x = 0, 3, 5$  and  $7$  at.%) RHEAs (named Mo0, Mo3, Mo5 and Mo7, respectively) were fabricated by vacuum arc melting. Ti, Zr, Nb, Ta, and Mo blocks with a purity of over 99.95 wt% were chosen as raw materials, followed by melting with a specific atomic ratio. The ingots were re-melted for 5 times to ensure the chemical homogeneity, and poured into a water-cooled copper mold ( $10 \times 10 \times 45$  mm). The actual chemical compositions of the ingots were detected by using X-ray fluorescence spectrometer (S8 TIGER), and the results were listed in Table 1.

### 2.2. Characterization

The metallographic samples ( $5 \times 5 \times 2$  mm) were cut from the ingots, followed by mechanically grinding, polishing and etching with Kroll acid (2 vol% HF + 3 vol%  $\text{HNO}_3$  + 95 vol%  $\text{C}_2\text{H}_5\text{OH}$ ). The phase composition was analyzed using X-ray diffractometer (XRD, D/MAX-2500), with  $2\theta$  of  $20^\circ$ – $90^\circ$  and scanning speed of  $5^\circ/\text{min}$ . The microstructure was analyzed using scanning electron microscope (SEM, Novanano SEM450), electron backscatter diffraction (EBSD, DigiView 5), and transmission electron microscope (TEM, FEI Tecnai F30). The EBSD samples of as-cast RHEAs were prepared by electrolytic polished with 60 vol%  $\text{CH}_3\text{OH}$ , 34 vol%  $\text{CH}_3(\text{CH}_2)_3\text{OH}$  and 6 vol%  $\text{HClO}_4$ , and the

electrolytic polished current and time were 30 V and 60 s, respectively. After nickel plating, the EBSD samples of the fracture sample were prepared using mechanical and vibratory polishing for 10 h (Vibro-MetTM2). The TEM samples with the size of  $\phi 5 \times 60 \mu\text{m}$  were thinned to electronic transparency through an ion thinning apparatus (Gatan 691). The thinning parameters were voltage of 5 KeV, incidence angle of  $6^\circ$ , and duration time of 120 min.

The tensile samples were machined to dumbbell shape with the size of  $2 \times 10 \times 45$  mm and measured by using MTS E45.305 universal electronic tester at room-temperature (RT). The compression samples were machined to a cylinder of  $\phi 8 \times 12$  mm, and were measured using the MTS E45.305 at 1173, 1273, and 1373 K. The tests for high-temperature compression were measured at a strain rate of  $10^{-3}/\text{s}$ . For each condition, three samples were tested to make sure the data was reliable. The density of the RHEA was calculated through the Archimedes principle.

The nanoindentation was performed using G200 nanoindenter quipped with a Berkovich tip, with load of 50 mN and loading rate of 5 mN/min. At least 100 indentations were performed to draw load-displacement ( $P-h$ ) curves and obtain pop-in points. The plasticity factor ( $\delta_A$ ), which is calculated through the  $P-h$  curve, can be used to evaluate the plasticity of RHEAs [20].

$$\delta_A = 1 - \frac{A_e}{A_t} \quad (1)$$

where  $A_e$  and  $A_t$  are the areas of the unloading and loading parts in the  $P-h$  curves, respectively.

## 3. Results and discussion

### 3.1. Microstructure

**Fig. 1a** displays XRD patterns of the  $(\text{Ti}_{42.5}\text{Zr}_{42.5}\text{Nb}_{10}\text{Ta}_5)_{100-x}\text{Mo}_x$  RHEAs. All the RHEAs are composed of a single BCC phase. As the Mo content increases, the (110) peak angle changes from  $36.84^\circ$  to  $37.34^\circ$ . In order to verify the phenomenon, the lattice constant ( $a$ ) of the BCC phase was calculated by using Bragg formula [21].

$$\sin^2 \theta = \frac{\lambda^2}{4a^2} (h^2 + k^2 + l^2) \quad (2)$$

where  $\theta$  is the incident angle and  $\lambda$  is the wavelength. The BCC lattice constants of the Mo0, Mo3, Mo5 and Mo7 samples are 3.4470, 3.4180, 3.4078 and 3.4033 Å, respectively. The changes of diffraction peaks and lattice parameters reflect severe lattice distortion of the BCC phase because of the solution of Mo atoms [22]. **Fig. 1b ~ e** shows microstructures of the Mo0 and Mo7 samples observed by using SEM and EBSD. Analyses of SEM images (**Fig. 1b** and **c**) reveal that all the RHEAs exhibit typical structures of intercrystalline dendrite, of which the size decreases with the increased Mo content.

From EBSD images (**Fig. 1d** and **e**), the Mo0 and Mo7 samples exhibit similar equiaxial BCC structures with different KAM distributions. **Fig. 1f** shows the grain size and average KAM value of the RHEAs. For the Mo0, Mo3, Mo5 and Mo7 samples, the average grain sizes are 31.26, 28.86, 24.32 and 15.57 μm. The addition of alloying elements obviously affects the grain growth self-diffusion activation energy is an important matter, where the addition of elements with high self-diffusion activation energy might be used to retard grain growth via the solute-drag effect [23]. The increased self-diffusion activation energy leads to the small grain size of RHEAs because of the addition of Mo with high self-diffusion activation energy (481.5 kJ/mol) [24]. For the Mo0, Mo3, Mo5 and Mo7 samples, the average KAM values are 0.1956, 0.2465, 0.2767 and 0.2934°, respectively. Generally, the higher the KAM value, the severer the lattice distortion [25]. These results reveal that increasing Mo content reduces grain size while increases lattice distortion of the RHEAs.

To better understand the phase component, valence electron con-

**Table 1**  
Real chemical compositions of the  $(\text{Ti}_{42.5}\text{Zr}_{42.5}\text{Nb}_{10}\text{Ta}_5)_{100-x}\text{Mo}_x$  RHEAs.

RHEAs	Chemical compositions (at.%)				
	Ti	Zr	Nb	Ta	Mo
Mo0	42.51	42.54	9.97	4.98	0.00
Mo3	41.21	41.23	9.71	4.87	2.98
Mo5	40.33	40.39	9.52	4.75	5.01
Mo7	39.55	39.54	9.26	4.63	7.02

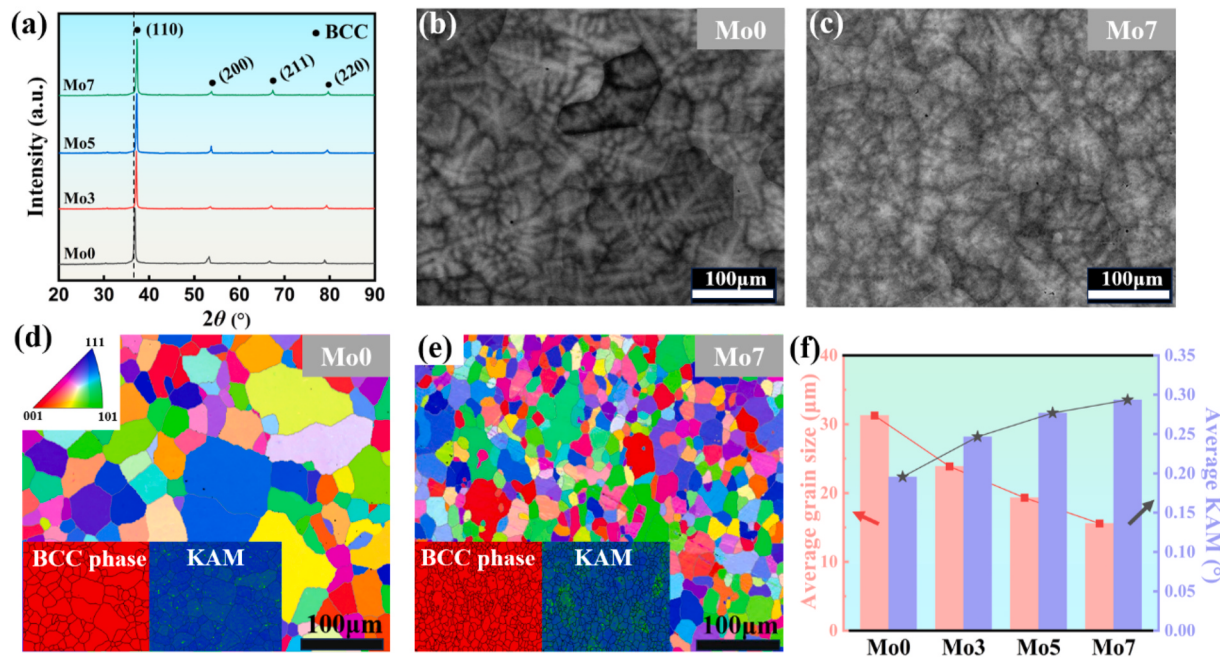


**Fig. 1.** (a) X-ray diffraction patterns of the  $(\text{Ti}_{42.5}\text{Zr}_{42.5}\text{Nb}_{10}\text{Ta}_5)_{100-x}\text{Mo}_x$  ( $x = 0, 3, 5$  and  $7$  at.%) RHEAs; (b ~ c) SEM images of the Mo0 and Mo7 RHEAs, (d ~ e) EBSD analyses of the Mo0 and Mo7 RHEAs, (f) Average Grain size and KAM value of the Mo0, Mo3, Mo5 and Mo7 RHEAs.

centration (VEC) and atomic radius difference parameter ( $\delta_r$ ) of the RHEAs were calculated based on empirical formulas [26,27].

$$\text{VEC} = \sum_{i=1}^n c_i (\text{VEC})_i \quad (3)$$

$$\delta_r = 100 \times \sqrt{\sum_{i=1}^n c_i \left(1 - \frac{r_i}{\bar{r}}\right)^2}, \bar{r} = \sum_{i=1}^n c_i r_i \quad (4)$$

where  $c_i$  and  $r_i$  are the atomic percentage and atomic radius of element  $i$ , respectively. Guo et al. [28] proposed that HEAs with the  $\text{VEC} \leq 6.87$  could consist of a single BCC phase. Zhang et al. [29] revealed that a stable single phase could form in HEAs with a criteria of  $\delta_r \leq 6.6$ . The calculated results are presented in Table 2. For the Mo0, Mo3, Mo5 and Mo7 samples, the VEC values are 4.15, 4.21, 4.25 and 4.28, and the  $\delta_r$  values are 4.92, 5.16, 5.31 and 5.45, respectively. It can be inferred that the single BCC phase existing in the  $(\text{Ti}_{42.5}\text{Zr}_{42.5}\text{Nb}_{10}\text{Ta}_5)_{100-x}\text{Mo}_x$  RHEAs is well consistent with the above predicted results.

Fig. 2a<sub>1</sub>~a<sub>2</sub> displays TEM bright-field images and selected area electron diffraction patterns (SAEDs) of the RHEAs. The lattice parameter of BCC phase in the Mo0 sample is  $a = b = c = 3.4327 \text{ \AA}$ , while that of the Mo5 sample is  $a = b = c = 3.4215 \text{ \AA}$ . High-resolution transmission electron microscopies (HRTEM) and geometric phase analyses (GPA) of the RHEAs are displayed in Fig. 2b<sub>1</sub>~b<sub>2</sub>. From the GPA analyses, the expansion (as marked by white arrows) along the xx and yy directions can be found in the RHEAs. Generally, the GPA value can reflect the distortion degree of lattice crystal because of microscopic strains existing in the atomic layer [30]. It is noticeable that severe distortion occurs in the lattice structure of the RHEAs. Due to isotropy at the as-cast state, the GPA values were counted along the xx direction to reflect the lattice distortion degree of RHEAs, and the results were displayed in

Fig. 2c<sub>1</sub>~c<sub>2</sub>. It can be known that the average GPA value of the Mo5 sample is larger than that of the Mo0 sample. In a word, the Mo addition facilitates the lattice distortion of BCC phase in the  $(\text{Ti}_{42.5}\text{Zr}_{42.5}\text{Nb}_{10}\text{Ta}_5)_{100-x}\text{Mo}_x$  RHEAs.

### 3.2. Mechanical properties

#### 3.2.1. Tensile mechanical property at RT

Fig. 3a presents the tensile plots of engineering stress-strain curves of the RHEAs at RT. The yield strength ( $\sigma_{ys}$ ), elongation ( $\epsilon$ ), and strength and plastic product ( $\sigma_{ys} \cdot \epsilon$ ) of the RHEAs are listed in Table 3. As the Mo content increases from 0 at.% to 7 at.%, the  $\sigma_{ys}$  of RHEAs increases from 670 MPa to 975 MPa with an amplification of 45.52 %, while the  $\epsilon$  and  $\sigma_{ys} \cdot \epsilon$  increase firstly and then decrease. By contrast, the Mo5 sample possesses the most excellent comprehensive mechanical properties, which have the values of  $\sigma_{ys}$ ,  $\epsilon$  and  $\sigma_{ys} \cdot \epsilon$  of 923 MPa, 21.81 % and 20130 MPa%, respectively. Fig. 3b illustrates the fractured morphologies of the Mo0, Mo5 and Mo7 tensile samples. The fractured surfaces of the Mo0 and Mo5 samples were completely covered with ductile dimples, reflecting a typical mechanism of ductile fracture. Meanwhile, the ductile dimple of the Mo5 sample is smaller than that of the Mo0 sample. Generally, the smaller ductile dimple possesses higher strength when the alloy exhibits similar plasticity levels [26,31]. However, the fracture surface of the Mo7 sample shows a brittle feature, where the microcracks spread all around, resulting in a low plasticity.

#### 3.2.2. Strengthening mechanism

In order to explore the strengthening mechanism, the theoretical yield strengths ( $\sigma_{ys}$ ) of the RHEAs based on grain-boundary strengthening ( $\sigma_{gb}$ ), solid-solution strengthening ( $\sigma_{ss}$ ), dislocation strengthening ( $\sigma_{ds}$ ) and second-phase strengthening ( $\sigma_{sp}$ ) [32].

$$\sigma_{ys} = \sigma_{gb} + \sigma_{ss} + \sigma_{ds} + \sigma_{sp} \quad (5)$$

In this paper, all the RHEAs are at as-cast condition, and the microstructures are single BCC solid solution, thus the  $\sigma_{ds}$  and  $\sigma_{sp}$  can be excluded. After simplification, the theoretical yield strengths of the RHEAs mainly depend on the  $\sigma_{gb}$  and  $\sigma_{ss}$  [33]. Here, the  $\sigma_{gb}$  can be calculated by the classical Hall-Petch equation [34].

**Table 2**

The VEC and  $\delta_r$  values of the  $(\text{Ti}_{42.5}\text{Zr}_{42.5}\text{Nb}_{10}\text{Ta}_5)_{100-x}\text{Mo}_x$  RHEAs.

Parameters	Mo0	Mo3	Mo5	Mo7
VEC	4.15	4.21	4.25	4.28
$\delta_r$ (%)	4.92	5.16	5.31	5.45

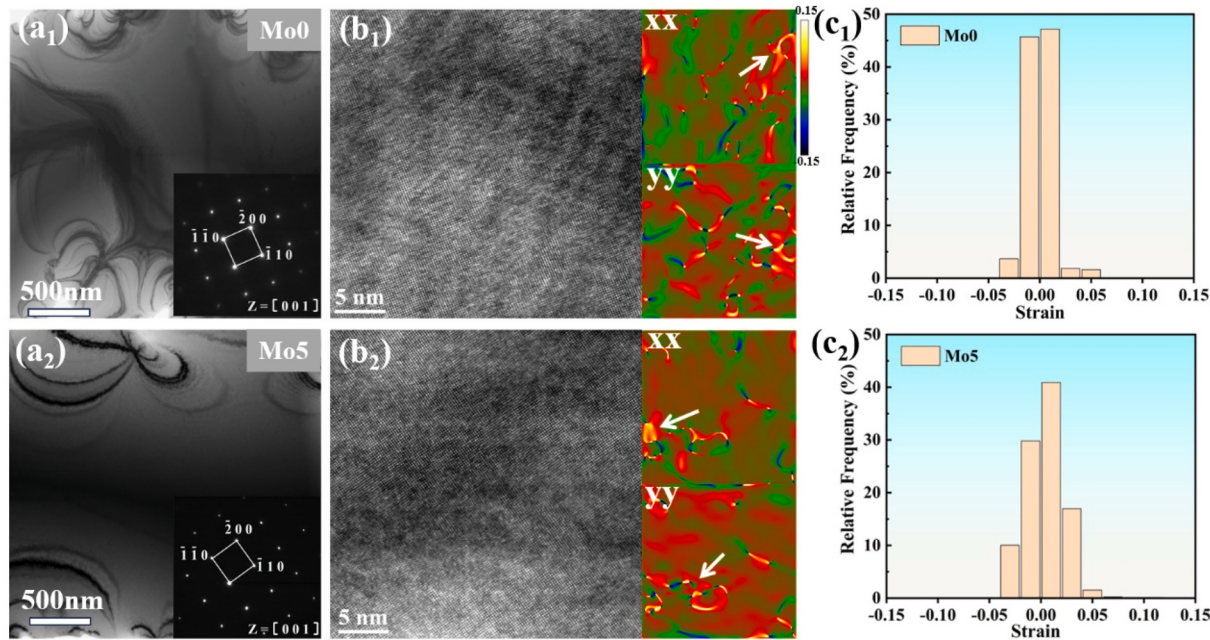


**Fig. 2.** The TEM analyses of the Mo0 (symbol 1) and Mo5 (symbol 2) RHEAs: (a) Bright-field images with corresponding SAED patterns; (b) HRTEM images with GPA analyses along the xx and yy directions; (c) Frequency distribution of GPA value along the xx direction.

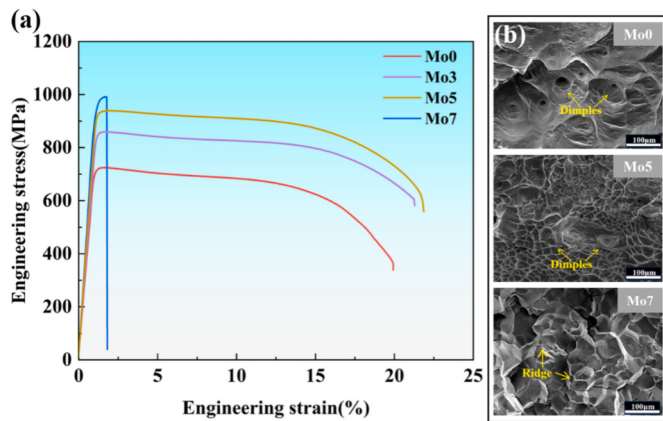


**Fig. 3.** (a) Tensile engineering stress-strain curves of the  $(\text{Ti}_{42.5}\text{Zr}_{42.5}\text{Nb}_{10}\text{Ta}_5)_{100-x}\text{Mo}_x$  ( $x = 0, 3, 5$  and  $7$  at.%) RHEAs, and (b) Fractured micromorphologies of the RHEAs.

**Table 3**  
Tensile properties of the  $(\text{Ti}_{42.5}\text{Zr}_{42.5}\text{Nb}_{10}\text{Ta}_5)_{100-x}\text{Mo}_x$  RHEAs.

RHEAs	Yield strength, $\sigma_{ys}$ (MPa)	Elongation, $\epsilon$ (%)	Strength and plasticity product, $\sigma_{ys} \cdot \epsilon$ (MPa%)
Mo0	670	19.92	13346
Mo3	828	21.26	17603
Mo5	923	21.81	20130
Mo7	975	1.73	1687

$$\sigma_{gb} = KD^{-\frac{1}{2}} \quad (6)$$

where  $K$  is the Hall-Petch coefficient with a value of  $430 \text{ MPa } \mu\text{m}^{-1/2}$  [35], and  $D$  is average grain size of the RHEAs.

As HEA is a new type of solid solution without clear distinction between solvent and solute, the solid-solution strengthening effect of HEA can be accessed through Toda-Caraballo model [36].

$$\sigma_{ss} = AGc^{\frac{2}{3}}f^{\frac{4}{3}} \quad (7)$$

$$f = \xi \left( (\delta G')^2 + \beta^2 \delta r^2 \right)^{\frac{1}{2}} \quad (8)$$

$$\delta G' = \frac{\delta G}{\left( 1 + \frac{|\delta G|}{2} \right)} \quad (9)$$

where  $c$  is solute atomic fraction,  $A$  is a scaling constant of 0.085 [32],  $G$  is shear modulus,  $f$  is mismatch parameter,  $\xi$  is the number of active slip systems,  $\beta$  is a constant value of 3, and  $\delta G$  and  $\delta r$  are shear moduli mismatch and atomic radius mismatch respectively. Generally, the solid-solution strengthening of alloy mainly depends on the lattice distortion dominated by shear modulus mismatch ( $\delta G$ ) and atomic radius mismatch ( $\delta r$ ) [37]. The  $\delta G$  and  $\delta r$  between the atoms  $i$  and  $j$  can be calculated by Eqs. (10) and (11) [38].

$$\delta r_{ij} = 2 \frac{r_i - r_j}{r_i + r_j} \quad (10)$$

$$\delta G_{ij} = 2 \frac{G_i - G_j}{G_i + G_j} \quad (11)$$

here,  $r_i$  and  $r_j$  means the atomic radius of pure metal  $i$  and  $j$ , respectively.  $G_i$  and  $G_j$  are the shear moduli of pure metal  $i$  and  $j$ , respectively. The average values of  $\delta G$  and  $\delta r$  of HEAs can be calculated by Eqs. (12) and (13).

$$\delta r^{\text{ave}} = \sum_i^n \sum_j^n c_i c_j \delta r_{ij} = (c_1, c_2, \dots, c_n) \begin{pmatrix} 0 & \delta r_{12} & \dots & \delta r_{1n} \\ \delta r_{21} & \ddots & \vdots & \delta r_{2n} \\ \vdots & \dots & 0 & \vdots \\ \delta r_{n1} & \delta r_{n2} & \dots & 0 \end{pmatrix} \begin{pmatrix} c_1 \\ c_2 \\ \vdots \\ c_n \end{pmatrix} \quad (12)$$

$$\begin{aligned} \delta G^{\text{ave}} &= \sum_i^n c_i \times \sum_j^n c_i c_j \delta G_{ij} \\ &= (c_1, c_2, \dots, c_n) \begin{pmatrix} 0 & \delta G_{12} & \dots & \delta G_{1n} \\ \delta G_{21} & \ddots & \vdots & \delta G_{2n} \\ \vdots & \dots & 0 & \vdots \\ \delta G_{n1} & \delta G_{n2} & \dots & 0 \end{pmatrix} \begin{pmatrix} c_1 \\ c_2 \\ \vdots \\ c_n \end{pmatrix} \end{aligned} \quad (13)$$

Assuming that RHEAs are composed of main elements  $i, j, k, l$  and  $m$ , and the mismatches caused by each element are similar. As a representative, the  $\delta G$  and  $\delta r$  induced by the  $i$  element were calculated by Eqs. (14) and (15).

$$\delta r_i = \frac{\delta r_{ijklm}^{\text{ave}} - \delta r_{jklm}^{\text{ave}}}{\delta c_i} \quad (14)$$

$$\delta G_i = \frac{\delta G_{ijklm}^{\text{ave}} - \delta G_{jklm}^{\text{ave}}}{\delta c_i} \quad (15)$$

Thus, the  $\sigma_{ss}$  value can be calculated and expressed by Eqs. (7), (8), (14) and (15), and simplified as Eq. (16).

$$\sigma_{ss} = \sum c_i \sigma_{ss}^i \quad (16)$$

For the Mo0, Mo3, Mo5 and Mo7 samples, the  $\sigma_{gb}$  values are 75, 80, 87, 108 MPa, and the  $\sigma_{ss}$  values are 580, 745, 825 and 903 MPa, respectively. Fig. 4 shows the contribution values of the  $\sigma_{gb}$  and  $\sigma_{ss}$  to the total yield strength of the RHEAs. It can be seen that the yield strength estimated by theoretical calculation well matches the experimental results. Meanwhile, the calculated results also prove that the ultra-high strengths of the BCC RHEAs are mainly dominated by solid-solution strengthening induced by the Mo addition.

### 3.2.3. Intrinsic plasticity or brittleness

Existing researches show that the majority of RHEAs exhibit brittleness at room temperature [39–41], while the Mo0, Mo3 and Mo5 samples show excellent tensile plasticity. In order to explore the plastic deformation behavior, different regions of the Mo5 tensile fracture were observed by using EBSD (Fig. 5). Here, areas a, b, c and d show the regions of 8, 6, 4 and 2 mm distances from the necking zone, respectively. The geometrically necessary dislocations (GNDs) of the Mo5 sample are shown in Fig. 5a~d, with the red regions showing high density dislocation. The increase of the GNDs occurs with the increase in strain. Meanwhile, it can be observed that high GNDs exist at the grain boundary. To be exact, the GND shows a sudden rise of  $1.2 \times 10^{15}/\text{m}^2$  at grain boundaries of the area d (Fig. 5e). This uneven GND distribution between grain boundary and intragranular will facilitate a high level of plastic strain accumulation [42]. The spots 1 and 2 were selected to

observe the changes in lattice orientation, where spots 1 and 2 represent different regions near the grain boundary of the same grain, respectively. The lattice orientation of the spot 1 is obviously different from that of the spot 2, indicating that the lattice around grain boundaries occurs in rotation to fit the strain distortion of grain boundaries during the tensile process [43]. Fig. 5f displays the length change of high-angle grain boundaries (HAGBs) from Fig. 5 a, b, c and d, where boundaries with  $>15^\circ$  misorientation are defined as HAGBs. The length value of HAGBs increases with it gets closer to the necking zone. It is shown that grain boundaries absorb dislocations to form HAGBs during the deformation process, resulting in promoted plastic deformation [44].

In general, the excellent tensile plasticity of  $\sim 20\%$  in the RHEAs is attributed to the following reasons. Firstly, lattice rotation occurs near the grain boundary. This lattice rotation leads to the introduction and increase of dislocations, resulting in coordinating the plastic deformation of RHEAs [45,46]. Secondly, Grain boundaries absorb dislocations to form HAGBs, resulting in promoted plastic deformation [44]. Thirdly, fine grain strengthening leads to an increase in the grain boundary. This means that there are more grain boundaries to accommodate dislocations under the same conditions [47].

Fig. 6 displays kernel average misorientations (KAM) of the Mo0, Mo5 and Mo7 fractures. KAM represents plastic deformation and strain energy of a specific region, and the brighter the specific region, the higher the KAM value [48]. From Fig. 6a, obvious tear or plastic deformation spread all around the Mo0 and Mo5 fractures, and more microcracks and severer local plastic deformation occur in the Mo5 fracture compared to the Mo0 fracture. The severer the plastic deformation, the longer the propagation time of microcracks, and the better the plasticity of the alloy [49]. Therefore, the Mo0 and Mo5 samples can possess high plasticity, and the plasticity of the Mo5 sample is higher than that of the Mo0 sample. By contrast, the Mo7 sample is a typical intergranular fracture, of which nearly no tears and local plastic deformation exist near the fracture. To quantify the plastic deformation degree of the RHEAs, the KAM values of the Mo0, Mo5 and Mo7 fractures were counted and shown in Fig. 6b. The average KAM value exhibits a trend of increases firstly and then decreases with the increased Mo content, which is well consistent with the plasticity (seen in Fig. 3). The brittle breakage observed in the Mo7 sample be caused by the rise of brittle-to-ductile transition temperature [50]. The brittle-to-ductile phenomenon is common for BCC RHEAs, such as NbMoTaW [8] and TiVNbTa [51] RHEAs, exhibiting typical temperature-dependent embrittlement at room-temperature.

### 3.2.4. Compression mechanical property at high-temperature

Considering the service environment of high-temperature materials, it is crucial to assess the mechanical properties of RHEAs under high-temperatures. Fig. 7a displays the compression plots of the true stress-strain curves for the Mo5 RHEA at 1173, 1273 and 1373 K. The yield strength (YS), specific yield strength (SYS) and fracture strain ( $\epsilon_f$ ) of the RHEAs are listed in Table 4. As shown in Fig. 7a, the true stress-strain curves for the Mo5 sample increases firstly and then decreases, followed by the steady-state. Some researchers have explained that the increase of the stress-strain curves are due to work hardening, and the decreases are attributed to dynamic recrystallization [52]. The yield strengths of the Mo5 sample are  $208 \pm 7$ ,  $96 \pm 5$ , and  $65 \pm 4$  MPa at 1173, 1273 and 1373 K, respectively. Meanwhile, the fracture strains of the Mo5 sample are greater than 60 % at the three temperatures. This ensures the excellent deformability of the RHEAs. The Mo5 RHEA exhibits high mechanical performance combined with low density property ( $6.56 \text{ g/cm}^3$ ). The specific yield strength of the Mo5 specimen is compared with other RHEAs, as shown in Fig. 7b. The relatively high specific yield strength of the Mo5 RHEA indicates that it may be have a wider potential for industrial applications.

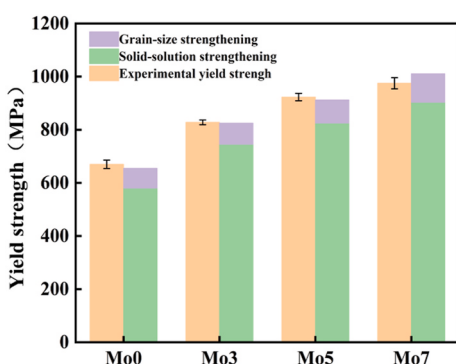


**Fig. 4.** A comparison of the yield strength from experiment and theoretical calculation in the  $(\text{Ti}_{42.5}\text{Zr}_{42.5}\text{Nb}_{10}\text{Ta}_5)_{100-x}\text{Mo}_x$  ( $x = 0, 3, 5$  and  $7$  at.%) RHEAs.

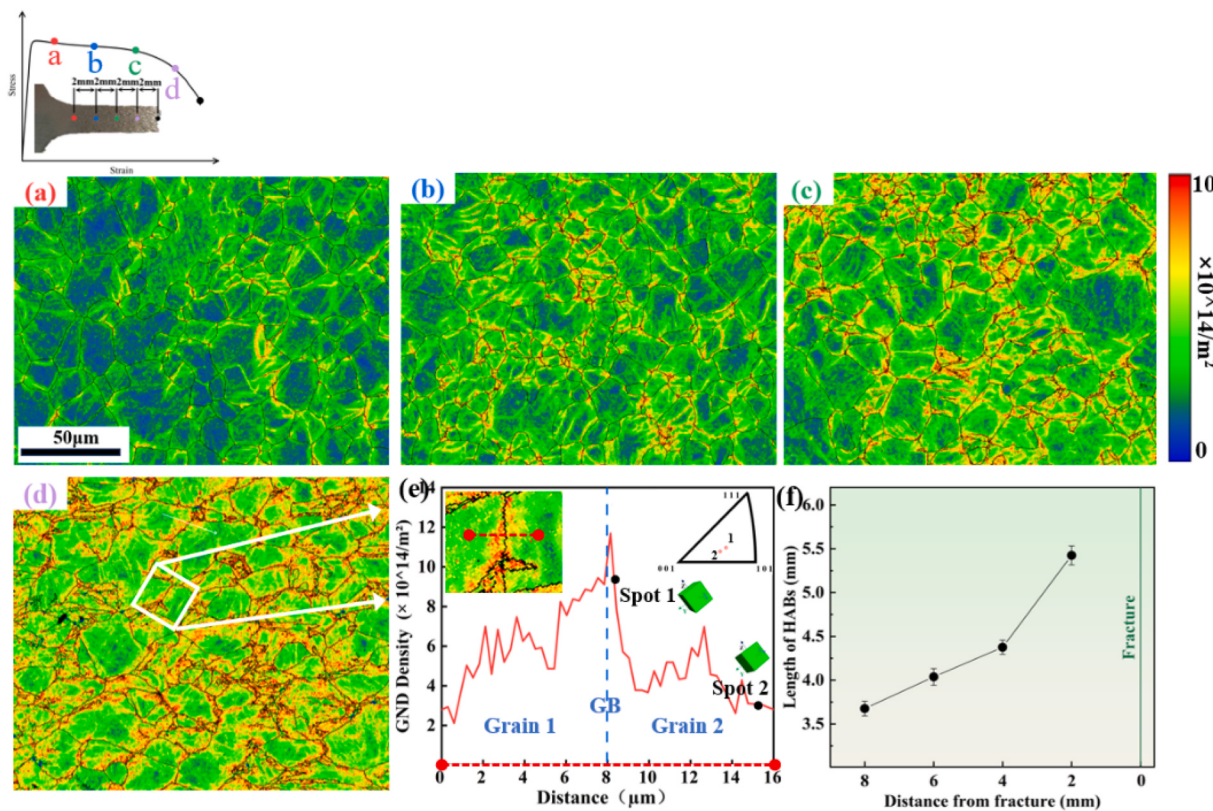


**Fig. 5.** The GNDs distribution maps for the Mo5 RHEAs: (a), (b), (c) and (d) GNDs maps correspond to 8, 6, 4 and 2 mm distances from the fracture, respectively; (e) GNDs density near the grain boundaries of area d; (f) IPF and orientation diagram.

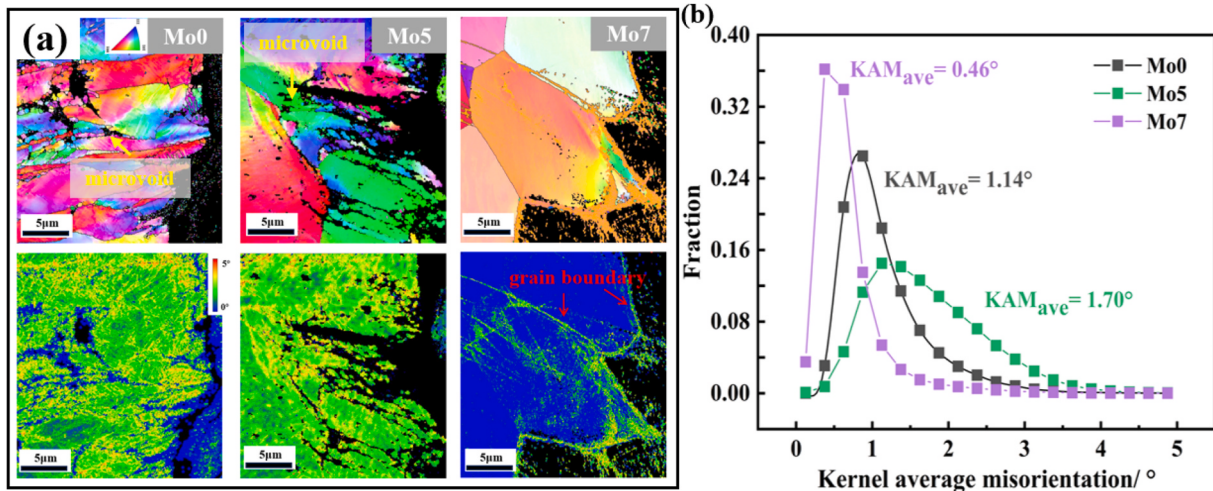


**Fig. 6.** EBSD investigations on the Mo0, Mo5 and Mo7 fractures after room-temperature tensile tests: (a) KAM distributions of the tensile fractures; (b) The KAM values.

### 3.3. Nanoindentation

The nucleation behavior of dislocation in the process of elastic-plastic transition can be evaluated by nanoindentation, which can also elucidate the change mechanism of mechanical properties [53,54]. Table 5 shows the nanomechanical properties of the  $(\text{Ti}_{42.5}\text{Zr}_{42.5}\text{Nb}_{10-x}\text{Ta}_5)_{100-x}\text{Mo}_x$  RHEAs, including nano-hardness ( $H$ ), elastic modulus ( $E$ ) and plasticity factor ( $\delta_A$ ). As Mo content increases from 0 at.% to 7 at.%, the  $H$ ,  $E$  and  $\delta_A$  values of the RHEAs change from  $2.33 \pm 0.30$  GPa,  $103 \pm 2.81$  GPa GPa and  $0.44$  to  $4.93 \pm 0.28$  GPa,  $129 \pm 3.19$  GPa and  $0.72$ , respectively. A higher  $\delta_A$  value correlates with better plasticity [20]. It

needs to be explained here that the  $\delta_A$  value of the Mo7 sample does not contradict to the tensile experimental result. This is because the plastic factor mainly reflects the BCC crystal, while the plasticity mainly depends on the grain boundary [55].

Moreover, the pop-in phenomena can be observed in the  $P-h$  curves (Fig. 8a). Pop-in is the starting point where the crystal begins to yield, and the initial stage of the  $P-h$  curve follows the Hertzian elastic theory [56].

$$P = \frac{4}{3}E_t R^2 h^2 \quad (17)$$

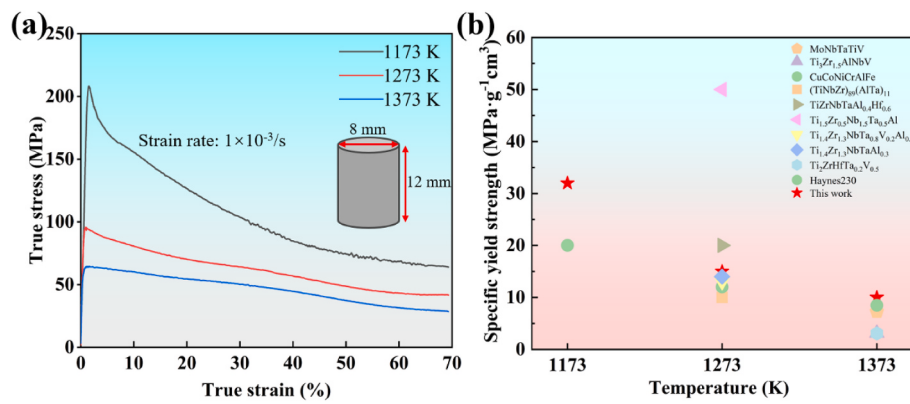


**Fig. 7.** Compressive properties of Mo5 RHEA at high temperature: (a) True stress-strain curves (b) Specific yield strength of the RHEAs in present work and others [11,53–58].

**Table 4**  
Compressive mechanical properties of the Mo5 RHEA.

	1173 K	1273 K	1373 K
YS (MPa)	$208 \pm 7$	$96 \pm 5$	$65 \pm 4$
SYS (MPa·g <sup>-1</sup> cm <sup>3</sup> )	32	15	10
$\varepsilon_c$ (%)	>70	>70	>70

**Table 5**  
Nanohardness, elastic modulus and plasticity factor of the (Ti<sub>42.5</sub>Zr<sub>42.5</sub>Nb<sub>10</sub>Ta<sub>5</sub>)<sub>100-x</sub>Mo<sub>x</sub> RHEAs.

RHEAs	H (GPa)	E (GPa)	$\delta_A$
Mo0	$2.33 \pm 0.30$	$103 \pm 2.81$	0.59
Mo3	$3.40 \pm 0.51$	$111 \pm 4.59$	0.66
Mo5	$4.44 \pm 0.22$	$117 \pm 2.43$	0.68
Mo7	$4.93 \pm 0.28$	$129 \pm 3.19$	0.72

where  $P$  is load ( $\mu\text{N}$ ),  $R$  is radius of the indenter tip ( $\sim 60 \text{ nm}$ ),  $h$  is the puncture depth of the indenter, and  $E_r$  is reduced modulus of the sample. The  $E_r$  can be calculated by Eq. (18).

$$\frac{1}{E_r} = \frac{1 - v_i^2}{E_i} + \frac{1 - v_s^2}{E_s} \quad (18)$$

here  $v_i$  ( $\sim 0.07$ ) and  $E_i$  ( $\sim 1141 \text{ GPa}$ ) represent the Young modulus and Poisson ratio of the diamond indenter, while  $v_s$  and  $E_s$  show the Young modulus and Poisson ratio of the sample, respectively. Through Eq. (18), the  $E_r$  of the four RHEAs is calculated by statistically fitting hundreds of pop-in points, and the fitting curves are shown in Fig. 8b. The  $E_r$  values of the Mo0, Mo3, Mo5 and Mo7 samples are  $98 \pm 3$ ,  $105 \pm 4$ ,  $120 \pm 6$  and  $132 \pm 6 \text{ MPa}$ , respectively. The larger the  $E_r$  value, the larger the atomic bonding, and the higher the yielding stress of alloy [57].

Combined with the obtained  $E_r$ , the maximum shear yielding stress ( $\tau_{\max}$ ) of the RHEAs was calculated based on the Hertz's contact theory [56,58].

$$\tau_{\max} = \frac{0.47}{\pi} \left( \frac{4E_r}{3R} \right)^{\frac{2}{3}} P^{\frac{1}{3}} \quad (19)$$

As the Mo content increases from 0 at.% to 7 at.%, the  $\tau_{\max}$  values of the RHEAs increase from 1.80–2.34 GPa to 2.67–4.83 GPa, as shown in Fig. 8c. Generally, the  $\tau_{\max}$  value is close to theoretical strength of a dislocation-free alloy [59,60]. Therefore, the  $\tau_{\max}$  is positively correlated with the yield strength of RHEAs, i.e. the higher the  $\tau_{\max}$  value, the larger the yield strength.

According to the theory proposed by Schuh et al. [61], the pop-in event is closely associated with the dislocation nucleation occurring in

the elastic-to-plastic transition process.

$$\ln(-\ln(1-f(P))) = \alpha P^{1/3} + \beta \quad (20)$$

where  $\alpha$  and  $\beta$  are the correlated constants,  $f$  is the cumulative probability of the pop-in event. Here, the  $\alpha$  is strongly correlated with the activation volume ( $v^*$ ) of dislocation nucleation as follows.

$$v^* = \frac{\pi}{0.47} \left( \frac{3R}{4E_r} \right)^{2/3} k_b T \alpha \quad (21)$$

where  $k_b$  is the Boltzmann constant, and  $T$  is the experimental temperature. The relationship between  $\ln(-\ln(1-f(P)))$  and  $P^{1/3}$  was plotted and shown in Fig. 8d. Based on Eqs. (20) and (21), the  $\alpha$  value depends on the slope of the fitting lines, by which the  $v^*$  can be deduced. The  $v^*$  values of the Mo0, Mo3, Mo5 and Mo7 samples are 0.7, 0.9, 1.0 and 1.1  $\Omega$  ( $\Omega$  is average atomic volume), respectively. The higher the  $v^*$  values, the more difficult the crystal plastic deform, and the larger the yield strength [62]. Therefore, the high Mo addition promotes large nanomechanical property for the RHEAs, which well corresponds to the tensile results (Fig. 3).

#### 4. Conclusions

The microstructure, mechanical properties and nanomechanical property of the (Ti<sub>42.5</sub>Zr<sub>42.5</sub>Nb<sub>10</sub>Ta<sub>5</sub>)<sub>100-x</sub>Mo<sub>x</sub> ( $x = 0, 3, 5$  and 7 at.%) RHEAs were systematically studied, and the main conclusions are as follows:

- All the RHEAs mainly consist of single a BCC phase. As the Mo content increases from 0 at.% to 7 at.%, the average grain sizes of RHEAs change from  $31.26 \mu\text{m}$  to  $15.57 \mu\text{m}$ , and the average KAM values very from  $0.1956^\circ$  to  $0.2934^\circ$ . The Mo addition facilitates grain refinement and lattice distortion for the RHEAs.
- As the Mo content increases, the yield strength of RHEAs increases from 670 MPa to 975 MPa, while the tensile plasticity increases firstly from 19.92% to 21.81% and then decreases to 1.7%. The RHEA with 5 at.% Mo possesses the most excellent comprehensive mechanical properties, of which the values of  $\sigma_{\text{ys}}$ ,  $\varepsilon$  and  $\sigma_{\text{ys}} \cdot \varepsilon$  of 923 MPa, 21.81% and 20130 MPa%, respectively.
- The yield strengths of the RHEA with 5 at.% Mo are  $208 \pm 7$ ,  $96 \pm 5$ , and  $65 \pm 4 \text{ MPa}$  at 1173, 1273 and 1373 K, respectively. The RHEA exhibits high mechanical performance combined with low density property ( $6.56 \text{ g/cm}^3$ ).
- With the increase of Mo content, the  $\sigma_{\text{gb}}$  values of RHEAs change from 75 MPa to 108 MPa, and the  $\sigma_{\text{ss}}$  values increase from 580 MPa to 903 MPa. The high strengths of the BCC RHEAs are mainly

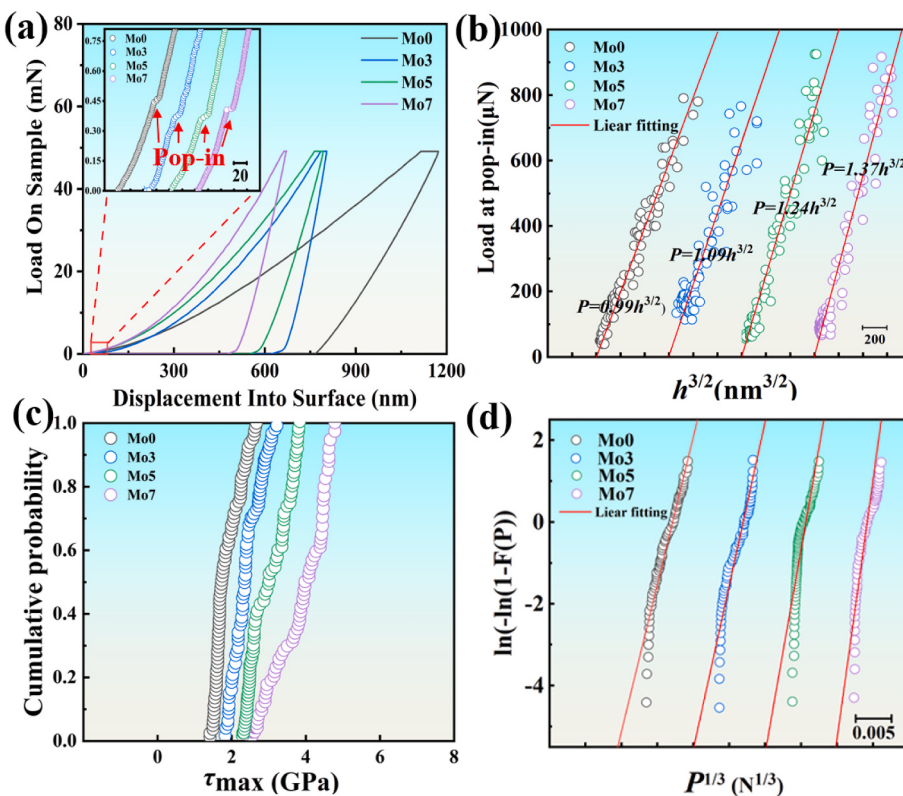


**Fig. 8.** Nanoindentation analyses of the  $(\text{Ti}_{42.5}\text{Zr}_{42.5}\text{Nb}_{10}\text{Ta}_5)_{100-x}\text{Mo}_x$  ( $x = 0, 3, 5$  and  $7$  at.%) RHEAs: (a)  $P$ - $h$  curves and magnified image of the pop-in events; (b) Statistical fitting hundreds of pop-in points; (c) The maximum shear stress underneath the indenter to trigger the Pop-in event; (d) Relationship between  $\ln(-\ln(1-f(P)))$  and  $P^{1/3}$ .

dominated by solid-solution strengthening caused by the Mo addition.

(5) The high Mo addition promotes large nanomechanical property for the RHEAs. After 7 at.% Mo addition, the reduced modulus  $E_r$ , maximum shear yielding stress  $\tau_{\max}$  and activation volume  $v^*$  increase to  $132 \pm 6$  MPa, 2.67–4.83 GPa and  $1.1 \Omega$ , respectively.

#### Declaration of competing interest

No conflict of interest exists in the submission of this manuscript, and manuscript is approved by all authors for publication. I would like to declare on behalf of my co-authors that the work described was original research that has not been published previously, and not under consideration for publication elsewhere, in whole or in part. All the authors listed have approved the manuscript that is enclosed.

#### Acknowledgment

This work was financially supported by the National Natural Science Foundation of China (Grant No. 52005217), University Research Platform and Research Projects of Guangdong Education Department (2022ZDZX3003), Guangdong Basic and Applied Basic Research Foundation (2024A1515012353 and 2023A1515220021), Guangzhou Science and technology planning project (2024A04J4063), and Natural Science Foundation of Guizhou Province of China (Grant Nos. ZK[2024] General 516 and 522).

#### References

- [1] Senkov ON, Senkova SV, Woodward C. Effect of aluminum on the microstructure and properties of two refractory high-entropy alloys. *Acta Mater* 2014;68:214–28.
- [2] Wang ZQ, Wu HH, Wu Y, Huang HL, Zhu XY, Zhang YJ, Zhu HH, Yuan XY, Chen Q, Wang SD, Liu XJ, Wang H, Jiang SH, Kim MJ, Lu ZP. Solving oxygen embrittlement of refractory high-entropy alloy via grain boundary engineering. *Mater Today* 2022;54:83–9.
- [3] Senkov ON, Miracle DB, Chaput KJ, Couzinie JP. Development and exploration of refractory high entropy alloys—a review. *J Mater Res* 2018;33(19):3092–128.
- [4] Srikant M, Annamalai AR, Muthuchamy A, Jen CP. A review of the latest developments in the field of refractory high-entropy alloys. *Crystals* 2021;11(6): 612.
- [5] Senkov ON, Wilks GB, Miracle DB, Chuang CP, Liaw PK. Refractory high-entropy alloys. *Intermetallics* 2010;18(9):1758–65.
- [6] Tian Y, Zhou W, Tan Q, Wu M, Qiao S, Zhu G, Dong A, Shu D, Sun B. A review of refractory high-entropy alloys. *Trans Nonferrous Metals Soc China* 2022;32(11): 3487–515.
- [7] Xu CH, Yu H, Xiao X, Zhang JW, Liao WB. Optimizing Al content to eliminate the brittle phase in lightweight TiZrNbTa0.1Alx refractory high-entropy alloys. *Appl Phys Lett* 2024;124(17).
- [8] Senkov ON, Wilks GB, Scott JM, Miracle DB. Mechanical properties of Nb<sub>25</sub>Mo<sub>25</sub>Ta<sub>25</sub>W<sub>25</sub> and V<sub>20</sub>Nb<sub>20</sub>Mo<sub>20</sub>Ta<sub>20</sub>W<sub>20</sub> refractory high entropy alloys. *Intermetallics* 2011;19:698–706.
- [9] Zhou J, Cheng Y, Chen Y, Liang X. Composition design and preparation process of refractory high-entropy alloys: a review. *Int J Refract Metals Hard Mater* 2022;105: 105836.
- [10] Han ZD, Chen N, Zhao SF, Fan LW, Yang GN, Shao Y, Yao KF. Effect of Ti additions on mechanical properties of NbMoTaW and VnbMoTaW refractory high entropy alloys. *Intermetallics* 2017;84:153–7.
- [11] Khan MA, Hamza M, Brecht J, Nazir Z, Qaisrani NA, Yasin G, Ahmad T, Liao WB, Liaw PK, Afifi MA. Development and characterization of a low-density TiNbZrAlTa refractory high entropy alloy with enhanced compressive strength and plasticity. *Mater Char* 2023;205:113301.
- [12] Lee C, Chou Y, Kim G, Gao MC, An K, Brecht J, Zhang C, Chen W, Poplawsky JD, Song G, Ren Y, Chou YC, Liaw PK. Lattice-distortion-Enhanced yield strength in a refractory high-entropy alloy. *Adv Mater* 2020;32(49):2004029.
- [13] Wang SP, Xu J. (TiZrNbTa)-Mo high-entropy alloys: dependence of microstructure and mechanical properties on Mo concentration and modeling of solid solution strengthening. *Intermetallics* 2018;95:59–72.
- [14] Hu Q, Guo S, Guo JL, Lu FF, Wang JW. Effect of Mo on high-temperature strength of refractory complex concentrated alloys: a perspective of electronegativity difference. *J Alloys Compd* 2022;906:164186.
- [15] Wang SP, Xu J. TiZrNbTaMo high-entropy alloy designed for orthopedic implants: as-cast microstructure and mechanical properties. *Mater Sci Eng C* 2017;73:80–9.
- [16] Juan CC, Tseng KK, Hsu WL, Tsai MH, Tsai CW, Lin CM, Chen SK, Lin SJ, Yeh JW. Solution strengthening of ductile refractory HfMo<sub>x</sub>NbTaTiZr high-entropy alloys. *Mater Lett* 2016;175:284–7.

- [17] Shao L, Xu CR, Ding N, Chen XT, Duan JM, Tang BY. The intrinsic mechanical properties of NbTaTiZr and the influence of alloying elements Mo and W: a first-principles study. *J Alloys Compd* 2022;911:165109.
- [18] Senkov ON, Daboku Tl, Butler TM, Titus MS, Philips NR, Payton EJ. High-temperature mechanical properties and oxidation behavior of Hf-27Ta and Hf-21Ta-21X (X is Nb, Mo or W) alloys. *Int J Refract Met H* 2021;96:105467.
- [19] Shao Y, Ma H, Wang YB. Effect of Mo addition on the microstructure and mechanical properties of CoCuFeNi high entropy alloy. *Metals* 2020;10(8):1017.
- [20] Yi Y, Li Q, Huang X, Zheng B, Liu Y, Tu X, Li W. Influence mechanism of  $K_2SO_4$  addition on microstructure, mechanical properties and abrasion resistance of Fe-2wt%B alloy. *Mater Des* 2021;197:109164.
- [21] Xie T, Jin F, Qin J, Qin L, Long S, Yi Y, Zhou S. Effects of La and Y on the microstructure and mechanical properties of NbMoTiVSi0.3 refractory high entropy alloys. *J Alloys Compd* 2023;931:167464.
- [22] Chen G, Yan H, Wang Z, Wang K, Yves NI, Tong Y. Effects of Mo content on the microstructure and mechanical properties of TiNbBzrMox high-entropy alloys. *J Alloys Compd* 2023;930:167373.
- [23] Zamani MR, Mirzadeh H, Malekan M, Cao SC, Yeh JW. Grain growth in high-entropy alloys (HEAs): a review. *High Entropy Alloys Mater* 2023;1:25–59.
- [24] Neumann G, Tujin C. Self-Diffusion and Impurity Diffusion in Group VI Metals. Self-diffusion and impurity diffusion pure metals: handbook of experimental data. Elsevier; 2009.
- [25] Guo BQ, Ray RK, Yoshida S, Bai Y, Tsuji N. In-situ observations of static recrystallization and texture formation in a cold-rolled CoCrFeMnNi high entropy alloy. *Scripta Mater* 2022;215:114706.
- [26] Sheikh S, Shafeie S, Hu Q, Ahlström J, Persson C, Veselý J, Zýka J, Klement U, Guo S. Alloy design for intrinsically ductile refractory high-entropy alloys. *J Appl Phys* 2016;120(16):164902.
- [27] Jing Y, Cui X, Jin G, Yang Y, Wen X, Guan Y, Zhang D. A new proposed parameter related with atomic size effect for predicting hardness of HEA coatings. *J Alloys Compd* 2021;856:158128.
- [28] Guo S, Ng C, Lu J, Liu CT. Effect of valence electron concentration on stability of fcc or bcc phase in high entropy alloys. *J Appl Phys* 2011;109(10):103505.
- [29] Zhang Y, Zhou YJ, Lin JP, Chen GL, Liaw PK. Solid-solution phase formation rules for multi-component alloys. *Adv Eng Mater* 2008;10(6):534–8.
- [30] Liu W, Yang Y, Liu Y, Huang S, Yu J, Ling J, Li Z, Yang Z, Xu C, Ding B, Li X, Gao Y, Jiang K, Lan S, Fu H, Fan B, Fu Y, Li J. Flexible solar cells based on foldable silicon wafers with blunted edges. *Nature* 2023;617:717–23.
- [31] Dirras G, Lilenstein L, Djemia P, Laurent-Brocq M, Tingaud D, Couzinié JP, Perrière L, Chauveau T, Guillot I. Elastic and plastic properties of as-cast equimolar TiHfZrTaNb high-entropy alloy. *Mater Sci Eng, A* 2016;654:30–8.
- [32] Lai W, Liu H, Yu X, Yi Y, Li W, Zhou S, Cui S, Wang X. A design of TiZr-rich body-centered cubic structured multi-principal element alloys with outstanding tensile strength and ductility. *Mater Sci Eng, A* 2021;813:141135.
- [33] Wang Z, Fang Q, Jin L, Liu B, Liu Y. Effect of lattice distortion on solid solution strengthening of BCC high-entropy alloys. *J Mater Sci Technol* 2018;34:349–54.
- [34] Sun SJ, Tian YZ, Lin HR, Dong XG, Wang YH, Wang ZJ, Zhang ZF. Temperature dependence of the HallePetch relationship in CoCrFeMnNi high-entropy alloy. *J Alloys Compd* 2019;806:992–8.
- [35] Courty FG, Kaufman M, Clarke AJ. Solid-solution strengthening in refractory high entropy alloys. *Acta Mater* 2019;175:66–81.
- [36] Toda-Caraballo I, Rivera-Díaz-del-Castillo PEJ. Modelling solid solution hardening in high entropy alloys. *Acta Mater* 2015;85:14–23.
- [37] Zhang Y, Zuo TT, Tang Z, Gao MC, Dahmen KA, Liaw PK, Lu ZP. Microstructures and properties of high-entropy alloys. *Prog Mater Sci* 2014;61:1–93.
- [38] Li L, Fang Q, Li J, Liu B, Liu Y, Liaw PK. Lattice-distortion dependent yield strength in high entropy alloys. *Mater Sci Eng, A* 2020;784:139323.
- [39] Li W, Xie D, Li D, Zhang Y, Gao Y, Liaw PK. Mechanical behavior of high-entropy alloys. *Prog Mater Sci* 2021;118:100777.
- [40] Senkov ON, Senkova SV, Miracle DB, Woodward C. Mechanical properties of low-density, refractory multi-principal element alloys of the Cr–Nb–Ti–V–Zr system. *Mater Sci Eng, A* 2013;565:51–62.
- [41] Senkov ON, Woodward CF. Microstructure and properties of a refractory NbCrMo<sub>0.5</sub>Ta<sub>0.5</sub>TiZr alloy. *Mater Sci Eng, A* 2011;529:311–20.
- [42] Gordon JV, Lim RE, Wilkin MJ, Pagan DC, Lebensohn RA, Rollett AD. Evaluating the grain-scale deformation behavior of a single-phase FCC high entropy alloy using synchrotron high energy diffraction microscopy. *Acta Mater* 2021;215:117120.
- [43] Poulsen HF, Margulies L, Schmidt S, Winther G. Lattice rotations of individual bulk grains. *Acta Mater* 2003;51(13):3821–30.
- [44] Ma X, Zhai H, Song L, Zhang W, Hu Y, Zhang Q. In situ study on plastic deformation mechanism of  $Al_{0.3}CoCrFeNi$  high-entropy alloys with different microstructures. *Mater Sci Eng, A* 2022;857:144134.
- [45] Chen P, Mao SC, Liu Y, Wang F, Zhang YF, Zhang Z, Han XD. In-situ EBSD study of the active slip systems and lattice rotation behavior of surface grains in aluminum alloy during tensile deformation. *Mater Sci Eng, A* 2013;580:114–24.
- [46] Joo SH, Kato H, Jang MJ, Moon J, Tsai CW, Yeh JW, Kim HS. Tensile deformation behavior and deformation twinning of an equimolar CoCrFeMnNi high-entropy alloy. *Mater Sci Eng, A* 2017;689:122–33.
- [47] Jeong HT, Kim WJ. Grain size and temperature effect on the tensile behavior and deformation mechanisms of non-equiaxitic Fe<sub>41</sub>Mn<sub>25</sub>Ni<sub>24</sub>Co<sub>8</sub>Cr<sub>2</sub> high entropy alloy. *J Mater Sci Technol* 2020;42:190–202.
- [48] Carneiro Í, Simões S. Recent advances in EBSD characterization of metals. *Metals* 2020;10(8):1097.
- [49] Kundu A, Field DP. Influence of plastic deformation heterogeneity on development of geometrically necessary dislocation density in dual phase steel. *Mater Sci Eng, A* 2016;667:435–43.
- [50] Wang SP, Ma E, Xu J. Notch fracture toughness of body-centered-cubic (TiZrNbTa) Mo high-entropy alloys. *Intermetallics* 2018;103:78–87.
- [51] Scales RJ, Armstrong DEJ, Wilkinson AJ, Li BS. On the brittle-to-ductile transition of the as-cast TiVNbTa refractory high-entropy alloy. *Materialia* 2020;14:100940.
- [52] Sakai T, Belyakov A, Kaibyshev R, Miura H, Jonas JJ. Dynamic and post-dynamic recrystallization under hot, cold and severe plastic deformation conditions. *Prog Mater Sci* 2014;60:130–207.
- [53] Wang P, Wu Y, Liu J, Wang H. Impacts of atomic scale lattice distortion on dislocation activity in high-entropy alloys. *Extreme Mech Lett* 2017;17:38–42.
- [54] Gan KF, Yan DS, Zhu SY, Li ZM. Interstitial effects on the incipient plasticity and dislocation behavior of a metastable high-entropy alloy: nanoindentation experiments and statistical modeling. *Acta Mater* 2021;206:116633.
- [55] Yan J, Fang W, Huang J, Zhang J, Chang R, Zhang X, Liu B, Feng J, Yin F. Plastic deformation mechanism of CoCr<sub>x</sub>Ni medium entropy alloys. *Mater Sci Eng, A* 2021;814:141181.
- [56] Mason JK, Lund AC, Schuh CA. Determining the activation energy and volume for the onset of plasticity during nanoindentation. *Phys Rev B* 2006;73(5):054102.
- [57] Hua D, Xia Q, Wang W, Zhou Q, Li S, Qian D, Shi J, Wang H. Atomistic insights into the deformation mechanism of a CoGrNi medium entropy alloy under nanoindentation. *Int J Plast* 2021;142:102997.
- [58] Mridha S, Das S, Aouadi S, Mukherjee S, Mishra RS. Nanomechanical behavior of CoCrFeMnNi high-entropy alloy. *Jom* 2015;67(10):2296–302.
- [59] Wu D, Nieh TG. Incipient plasticity and dislocation nucleation in body-centered cubic chromium. *Mater Sci Eng, A* 2014;609:110–5.
- [60] Wang L, Bei H, Li TL, Gao YF, George EP, Nieh TG. Determining the activation energies and slip systems for dislocation nucleation in body-centered cubic Mo and face-centered cubic Ni single crystals. *Scripta Mater* 2011;65(3):179–82.
- [61] Schuh CA, Lund AC. Application of nucleation theory to the rate dependence of incipient plasticity during nanoindentation. *J Mater Res* 2011;19(7):2152–8.
- [62] Li J, Fang Q, Liu B, Liu Y, Liu Y. Atomic-scale analysis of nanoindentation behavior of high-entropy alloy. *J Micromech Mol Phys* 2016;1(1):1650001.